Title

Time-gated single photon counting enables separation of CARS microscopy data from multiphoton-excited tissue autofluorescence

Journal

Optics Express, 15(25)

ISSN

1094-4087

Authors

Ly, Sonny
McNerney, Gregory
Chan, James
et al.

Publication Date

2007-12-01

Peer reviewed

Time-gated single photon counting enables separation of CARS microscopy data from multiphoton-excited tissue autofluorescence

Sonny Ly[1,2,†], Gregory McNerney[1,3,†], Samantha Fore[1], James Chan[1,4], and Thomas Huser[1,5,*]

[1]*NSF Center for Biophotonics Science and Technology, University of California, Davis, Sacramento, CA 95817, USA*
[2]*Department of Applied Science, University of California, Davis, Davis, CA 95616, USA*
[3]*Biophysics Graduate Group, University of California, Davis, Davis, CA 95616, USA*
[4]*Physical Sciences Directorate, Lawrence Livermore National Laboratory, Livermore, CA 94550, USA*
[5]*Department of Internal Medicine, University of California, Davis, Sacramento, CA 95817, USA*
[†]*these authors contributed equally to this work*
[*]Corresponding author: *trhuser@ucdavis.edu*

http://www.cbst.ucdavis.edu

Abstract: We demonstrate time-gated confocal imaging as a means to separate coherent anti-Stokes Raman scattering (CARS) microscopy data from multi-photon excited endogenous fluorescence in tissue. CARS is a quasi-instantaneous process and its signal decay time is only limited by the system's instrument response function (IRF). Signals due to two-photon-excited (TPE) tissue autofluorescence with excited state lifetimes on the nanosecond scale can be identified and separated from the CARS signal by employing time-gating techniques. We demonstrate this improved contrast on the example of CARS microscopy of intact roots of plant seedlings as well as on rat arterial tissue.

OCIS codes: (180.4315) Nonlinear microscopy; (170.6920) Time-resolved imaging; (190.5650) Raman effect.

References

1. C. L. Evans, E. O. Potma, M. Puoris'haag, D. Cote, C. P. Lin, and X. S. Xie, "Chemical imaging of tissue in vivo with video-rate coherent anti-Stokes Raman scattering microscopy," PNAS **102**, 16807-16812 (2005).
2. T. B. Huff, and J. X. Cheng, "In vivo coherent anti-Stokes Raman scattering imaging of sciatic nerve tissue," J. Microsc. **225**, 175-182 (2007).
3. H. Kano, and H. Hamaguchi, "Vibrationally resonant imaging of a single living cell by supercontinuum-based multiplex coherent anti-Stokes Raman scattering microspectroscopy," Opt. Express **13**, 1322- 1327 (2005).
4. O. Burkacky, A. Zumbusch, C. Brackmann, and A. Enejder, "Dual-pump coherent anti-Stokes-Raman scattering microscopy," Opt. Lett. **31**, 3656-3658 (2006).
5. X. L. Nan, E. O. Potma, and X. S. Xie, "Nonperturbative chemical imaging of organelle transport in living cells with coherent anti-stokes Raman scattering microscopy," Biophys. J. **91**, 728-735 (2006).
6. L. Tong, Y. Lu, R. J. Lee, and J. X. Cheng, "Imaging receptor-mediated endocytosis with a polymeric nanoparticle-based coherent anti-stokes raman scattering probe," J. Phys. Chem. B **111**, 9980-9985 (2007).
7. H. F. Wang, Y. Fu, P. Zickmund, R. Y. Shi, and J. X. Cheng, "Coherent anti-stokes Raman scattering imaging of axonal myelin in live spinal tissues," Biophys. J. **89**, 581-591 (2005).
8. J. X. Cheng, Y. K. Jia, G. F. Zheng, and X. S. Xie, "Laser-scanning coherent anti-stokes Raman scattering microscopy and applications to cell biology," Biophys. J. **83**, 502-509 (2002).
9. J. X. Cheng, A. Volkmer, and X. S. Xie, "Theoretical and experimental characterization of coherent anti-Stokes Raman scattering microscopy," J. Opt. Soc. Am. B **19**, 1363-1375 (2002)
10. J. X. Cheng, and X. S. Xie, "Coherent anti-Stokes Raman scattering microscopy: Instrumentation, theory, and applications," J. Phys. Chem. B **108**, 827-840 (2004).

11. A. Volkmer, J. X. Cheng, and X. S. Xie, "Vibrational imaging with high sensitivity via epidetected coherent anti-Stokes Raman scattering microscopy," Phys. Rev. Lett. **8702**, 4 (2001).
12. N. Djaker, P. F. Lenne, D. Marguet, A. Colonna, C. Hadjur, and H. Rigneault, "Coherent anti-Stokes Raman scattering microscopy (CARS): Instrumentation and applications," Nuc. Instr. Meth. Phys. **571**, 177-181 (2007).
13. L. G. Rodriguez, S. J. Lockett, and G. R. Holtom, "Coherent anti-stokes Raman scattering microscopy: A biological review," Cytometry A **69A**, 779-791 (2006).
14. G. J. Puppels, F. F. M. Demul, C. Otto, J. Greve, M. Robertnicoud, D. J. Arndtjovin, and T. M. Jovin, "Studying Single Living Cells and Chromosomes by Confocal Raman Microspectroscopy," Nature **347**, 301-303 (1990).
15. J. W. Chan, A. P. Esposito, C. E. Talley, C. W. Hollars, S. M. Lane, and T. Huser, "Reagentless identification of single bacterial spores in aqueous solution by confocal laser tweezers Raman spectroscopy," Anal. Chem. **76**, 599-603 (2004).
16. N. J. Crane, M. D. Morris, M. A. Ignelzi, and G. G. Yu, "Raman imaging demonstrates FGF2-induced craniosynostosis in mouse calvaria," J. Biomed. Opt. **10**, 8 (2005).
17. M. Kazanci, H. D. Wagner, N. I. Manjubala, H. S. Gupta, E. Paschalis, P. Roschger, and P. Fratzl, "Raman imaging of two orthogonal planes within cortical bone," Bone **41**, 456-461 (2007).
18. G. J. Zhang, D. J. Moore, C. R. Flach, and R. Mendelsohn, "Vibrational microscopy and imaging of skin: from single cells to intact tissue," Anal. Bioanal. Chem. **387**, 1591-1599 (2007).
19. G. J. Zhang, D. J. Moore, K. B. Sloan, C. R. Flach, and R. Mendelsohn, "Imaging the prodrug-to-drug transformation of a 5-fluorouracil derivative in skin by confocal Raman microscopy," J. Invest. Dermatol. **127**, 1205-1209 (2007).
20. M. D. Duncan, J. Reintjes, and T. J. Manuccia, "Scanning Coherent Anti-Stokes Raman Microscope," Opt. Lett. **7**, 350-352 (1982).
21. A. Zumbusch, G. R. Holtom, and X. S. Xie, "Three-dimensional vibrational imaging by coherent anti-Stokes Raman scattering," Phys. Rev. Lett. **82**, 4142-4145 (1999).
22. K. Konig, and I. Riemann, "High-resolution multiphoton tomography of human skin with subcellular spatial resolution and picosecond time resolution," J. Biomed. Opt. **8**, 432-439 (2003).
23. K. Konig, K. Schenke-Layland, I. Riemann, and U. A. Stock, "Multiphoton autofluorescence imaging of intratissue elastic fibers," Biomaterials **26**, 495-500 (2005).
24. M. C. Skala, J. M. Squirrell, K. M. Vrotsos, V. C. Eickhoff, A. Gendron-Fitzpatrick, K. W. Eliceiri, and N. Ramanujam, "Multiphoton microscopy of endogenous fluorescence differentiates normal, precancerous, and cancerous squamous epithelial tissues," Cancer Res. **65**, 1180-1186 (2005).
25. J. A. Palero, H. S. de Bruijn, A. van der Ploeg-van den Heuvel, H. Sterenborg, and H. C. Gerritsen, "In vivo nonlinear spectral imaging in mouse skin," Opt. Express **14**, 4395-4402 (2006).
26. J. M. Piepmeier, C. Y. Liu, and E. Neuwelt, "Multiphoton excitation of autofluorescence for microscopy of glioma tissue - Comments," Neurosurgery **58**, 767-767 (2006).
27. J. A. Palero, H. S. de Bruijn, A. V. van den Heuvel, H. Sterenborg, and H. C. Gerritsen, "Spectrally resolved multiphoton imaging of in vivo and excised mouse skin tissues," Biophys. J. **93**, 992-1007 (2007).
28. E. S. Lee, J. Y. Lee, and Y. S. Yoo, "Nonlinear optical interference of two successive coherent anti-Stokes Raman scattering signals for biological imaging applications," J. Biomed. Opt. **12**, 5 (2007).
29. E. O. Potma, C. L. Evans, and X. S. Xie, "Heterodyne coherent anti-Stokes Raman scattering (CARS) imaging," Opt. Lett. **31**, 241-243 (2006).
30. I. Toytman, K. Cohn, T. Smith, D. Simanovskii, and D. Palanker, "Wide-field coherent anti-Stokes Raman scattering microscopy with non-phase-matching illumination," Opt. Lett. **32**, 1941-1943 (2007).
31. W. Becker, A. Bergmann, M. A. Hink, K. Konig, K. Benndorf, and C. Biskup, "Fluorescence lifetime imaging by time-correlated single-photon counting," Microsc. Res. and Technique **63**, 58-66 (2004).
32. R. R. Duncan, A. Bergmann, M. A. Cousin, D. K. Apps, and M. J. Shipston, "Multi-dimensional time-correlated single photon counting (TCSPC) fluorescence lifetime imaging microscopy (FLIM) to detect FRET in cells," J. Microsc. **215**, 1-12 (2004).
33. M. Peter, and S. M. Ameer-Beg, "Imaging molecular interactions by multiphoton FLIM," Biology of the Cell **96**, 231-236 (2004).
34. K. Suhling, P. M. W. French, and D. Phillips, "Time-resolved fluorescence microscopy," Photochem. Photobiol. Sci. **4**, 13-22 (2005).

1. Introduction

While still in early stages of adoption by cell biologists and medical researchers, coherent anti-Stokes Raman scattering (CARS) microscopy has emerged as a powerful new imaging modality for applications in cell biology and disease characterization [1-7]. As a microscopy

technique, it enables imaging with diffraction-limited spatial resolution, high speed, and high chemical selectivity - similar to confocal microscopy - but without the need for fluorescent labels [8-13]. CARS microscopy is a mergence of Raman scattering and nonlinear optical microscopy. Raman scattering probes the strength and composition of molecular bonds through inelastic light scattering [14]. Different molecular bonds exhibit different vibrational frequencies so that monitoring these allows for the label-free probing of specific molecules, such as proteins, DNA, RNA, and lipids, and their distribution within tissue or even within a single cell [15]. Traditional Raman scattering microscopy based on spontaneous light scattering has to cope with extremely weak signals, which, when used in an imaging application requires typical acquisition times of up to several hours [16-19]. CARS microscopy overcomes this limitation by using coherent excitation of molecular bonds to increase the signal strength by several orders of magnitude. Here, two laser beams with energies ω_p and ω_S are tuned so that their difference in energy matches a specific Raman-active vibration (ω_{vib}). A nonlinear optical process drives molecules through the Raman vibration, and produces an anti-Stokes signal at $\omega_{CARS} = 2\omega_p - \omega_s = \omega_p + \omega_{vib}$. This signal is the vibrational marker providing chemical contrast for CARS imaging. If the two laser beams are tightly focused, the stringent phase-matching condition is relaxed while simultaneously creating the high electric field strength required to induce a CARS process. The CARS signal, by and large, is then only generated at that focal point. Raster-scanning this focal point across the sample then produces 3-dimensional vibrational images with diffraction-limited resolution (<1 μm).

To improve the CARS signal over any fluorescence background, a number of developments were made from its original form [20], such as shifting the excitation laser wavelength to the near-infrared [21]. Unfortunately, however, during imaging at the tissue level, short-pulsed near-infrared laser illumination also leads to two-photon-induced excitation of endogenous fluorescence – especially at the peak pulse energies needed to generate sufficient CARS or other nonlinear signals [22-27]. Depending on the type of tissue, this background fluorescence can exhibit significant spectral overlap with the CARS signal and often mask it. This is particularly true for chlorophyll-rich plant tissues. Chlorophyll exhibits strong fluorescence with a peak emission at ~ 670 nm, which overlaps with most CARS signals obtained by using a combination of laser wavelengths around 800 nm and 1064 nm as done in most of the current CARS microscopy setups [4, 28-30]. Other tissue types, in particular tissues that are in contact with blood, have other sources of broadband autofluorescence in a similar wavelength range, which stem from e.g. porphyrins and heme. To date, suppressing these autofluorescence signals in CARS imaging has been limited to the use of narrow bandpass filters centered around the CARS signal. This scheme alone has several limitations: 1) the spectral width of bandpass filters is often larger than the CARS spectral width, leading to excess background bleed-through, 2) any remaining fluorescence signal on top of the CARS spectral position still cannot be suppressed, and 3) using narrow bandpass filters greatly restricts the ability to tune between a range of Raman modes without switching filters. Alternatively, a potential technique to enhance the CARS contrast is to perform background subtraction of autofluorescence from CARS by acquiring separate fluorescence images with just one laser and subtracting these by using imaging software, but this method is tedious and time consuming.

Here, we implement an entirely different approach in separating CARS signals from tissue TPE autofluorescence. In Raman scattering and CARS, the molecule is excited to a virtual state, an unstable state with a large energy uncertainty, resulting in a quasi-instantaneous decay time (<1 ps). This distinguishes it well from the typical nanosecond electronic excited state lifetimes that are characteristic of fluorescence emission. By implementing a time-correlated single photon counting (TCSPC) detection scheme similar to what has been previously reported for fluorescence lifetime imaging (FLIM) [31-34], we are able to use the photon arrival time information to discriminate between the quasi-instantaneous CARS photons and the delayed TPE autofluorescence photons, thereby improving the quality of the CARS images.

2. Materials and methods

2.1. CARS microscope

Our CARS microscope is set up in the epi-detection mode as shown in Fig. 1a. The pump laser source is provided by a 1064 nm Nd:YVO_4 laser (Picotrain, High Q Laser, Austria) with 10 W average power and 7 ps pulse width at 76 Mhz repetition rate. A large portion of the laser power, 9W, is used to synchronously pump an optical parametric oscillator (OPO – Levante, APE, Berlin, Germany), generating approximately 1.5 W of OPO average power with 5 ps pulse width, and wavelengths tunable from 770 nm to 960 nm. The remaining portion of the Nd:YVO_4 laser source (~1 W) is used as the Stokes beam. The 1064 nm Stokes beam is passed through a 100 mm optical delay stage and collimated by a lens pair before being combined with the OPO pump beam by a dichroic mirror (Chroma Technology, Rockingham, VT). The combined laser beams are then delivered to the rear entrance port of an inverted optical microscope (IX71, Olympus, Center Valley, PA) through a periscope. The CARS beams are reflected by a 750 nm short pass dichroic mirror (Chroma Technology, Rockingham, VT) and sent to the back-aperture of a 1.2NA, 60X water immersion objective, (Olympus, Center Valley, PA) to form a diffraction-limited spot at the sample. The epi-CARS signal is collected by the same microscope objective, spectrally separated from the excitation sources by the dichroic mirror and a set of bandpass filters, i.e. a multiphoton short-pass filter (FF-01-750, Semrock, Rochester, NY) and a 40 nm wide bandpass filter (#42-7377, Ealing Catalog, Inc., Rocklin, CA) around 660 nm, before being focused onto a single photon counting avalanche photodiode (SPAD, SPCM-AQR 14, Perkin-Elmer, Waltham, MA). A portion of the CARS signal is also sent to a spectrometer (Acton SpectraPro 2300i, PI Acton, Trenton, NJ) equipped with a back-illuminated deep-depletion charge-coupled device (CCD) camera (PIXIS 100BR, PI Acton, Trenton, NJ). For all images shown in this report, the OPO wavelength was tuned to 816.8 nm to match the aliphatic C-H stretch mode at 2845 cm^{-1} corresponding to a CARS signal at 658 nm.

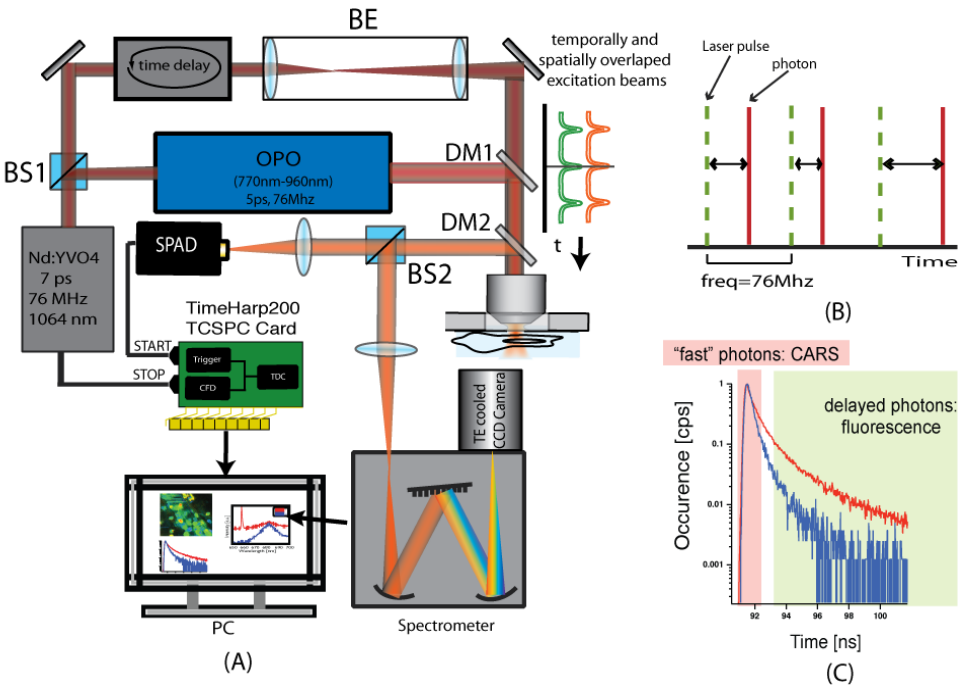

Fig. 1. (A) Schematics of our experimental CARS microscopy system. An optical parametric oscillator is synchronously pumped by a Nd:YVO_4 laser (10W, 7 ps, 1064 nm, 76 MHz) to produce the excitation beam, while the Nd:YVO_4 laser provides the probe beam. CARS signals are detected in epi-mode by a single photon counting avalanche photodiode (SPAD). BS: beam

splitter, DM: dichroic mirror, BE: beam expander, OPO: optical parametric oscillator, TCSPC: time-correlated single photon couting, PC: personal computer. (B) TCSPC concept: the arrival time of a photon is detected with 35 ps resolution with respect to the laser pulse. (C) Photon arrival time distribution histogram of the 2845 cm^{-1} CARS signal from aliphatic C-H bonds generated in rat artery by scanning the CARS beams and collecting photon arrival time data for every pixel, which are fitted by a single exponential decay function. The fit values for each photon arrival time are shown in the distribution histogram. The majority of photons arrives with a time constant of 310 ps, which reflects the instrument response function of our system – limited by the timing jitter of the SPAD. The microscopic photon arrival time is determined by the TimeHarp200 histogramming electronics, whereby the start-stop times are binned to a 4096 channel histogram with an adjustable resolution per channel and a minimum resolution corresponding to ~ 30 ps. CARS and TPE fluorescence images are generated by the SymphoTime software by setting the respective time-gates, i.e. by selecting a subset of photons collected during a given time range within the microscopic photon arrival (TCSPC) time window, corresponding to CARS only and TPE fluorescence photons, respectively.

2.2. Imaging electronics

CARS images are generated by translating the microscope objective across the sample in the lateral x-y, and axial z-plane using a closed-loop controlled piezoelectric motion stage (Polytec PI). Scan control of the piezo stage is provided by the SymPhoTime software package (Picoquant GmbH, Berlin, Germany). Signals from the SPAD and reference photo diode are acquired by a time-correlated single photon counting board (TCSPC, TimeHarp 200, Picoquant GmbH, Berlin, Germany). By utilizing SPADs and TCSPC electronics, macroscopic (absolute timescale, recorded with 100 ns precision) and microscopic (relative timescale in the picosecond to nanosecond range, 35 ps minimum time-resolution) photon arrival times are recorded for every photon detected by the electronics with respect to the laser excitation pulse. This is achieved by acquiring data in reverse START-STOP mode. The START pulse is generated by the SPAD while the STOP (or SYNC) pulse is provided by a direct sync output from the Nd:YVO_4 via an internal photodiode. Furthermore, operation of the TimeHarp200 board in time-tagged time-resolved (TTTR) mode allows for the full time-resolved analysis of collected photon events over the time scale of picoseconds to nanoseconds, as well as synchronization to the piezo-scanner for image formation. The microscopic photon arrival time enables us to employ software time-gating to display only those photons that were detected within a specified time window. From here on out, whenever we refer to *arrival time* in the text, we mean *microscopic arrival time*. The macroscopic photon arrival time, on the other hand, enables the reconstruction of images (TPE fluorescence and CARS). It should be noted that because of the high repetition rate of the laser system (76 MHz), the TCSPC time window between adjacent pulses is limited to ~13 ns for the applications shown in this paper. This can be expanded through the use of optoelectronic pulse pickers.

2.3. Sample preparation

Seedlings of *Arabidopsis thaliana* were prepared by growing them in the dark for 1 week, then placing one seedling on a 0.17 mm thick coverslip mounted in an Attofluor cell chamber (Invitrogen, Inc., Eugene, Oregon), and immersing the plant in Dulbecco's phosphate buffered saline solution. The intact, living plant seedling was used for CARS imaging.

A section of the main thoracic aorta in the heart, running along the side of the esophagus and behind the lungs of a healthy young rat was surgically removed. It was then cut in the cross section plane of 1 mm slices and stored in a flask filled with cold saline solution with 0.9% sodium chloride content, before being transferred to a microscope cover slip.

3. Results

3.1. Arabidopsis thaliana plant sample

A dark-grown seedling of *Arabidopsis thaliana* was imaged in our CARS system near the roots of the plant. Dark-grown seedlings develop few to no chloroplasts, which should reduce the plant tissue fluorescence significantly. Further minimization of autofluorescence

background is achieved by imaging near the roots rather than the leaves of the plant. Fig. 2(a) shows a transmitted light micrograph of the lower stem ("hypocotyls") near the roots of the seedling. This micrograph provides little contrast of the sample, except for some cell membranes. The arrows shown in the figure point to parts of the image that are also shown in the corresponding CARS image in Fig. 2(b). For CARS microscopic image acquisition of the seedling, the OPO pump laser was tuned to 816.8 nm using 35 mW average power at the sample, while the Nd:YVO_4 probe laser was set to 11 mW at the sample. The beams were focused onto the sample using a 60X 1.20 NA UPlanSApo water immersion objective (Olympus America, Center Valley, PA). The 256 x 256 pixel CARS image was acquired using a 2 ms dwell time per pixel in a 40 µm x 40 µm sample area. This image shows significantly more contrast than the transmitted light image, allowing for the identification of vesicles and organelles within the plant. Spectra were taken following the imaging using 0.3 s exposure times in various locations, two of which are shown in Fig. 2(c) and correspond to the locations highlighted in Fig. 2(b). As can be seen from these spectra, location (i) exhibits a relatively significant CARS signal as evidenced by the intense, spectrally narrow peak around 658 nm. This signal sits on top of a broader fluorescence peak with a maximum at ~ 680 nm. The spectrum obtained from location (ii), on the other hand, is dominated by the fluorescence signal and shows a very small CARS contribution.

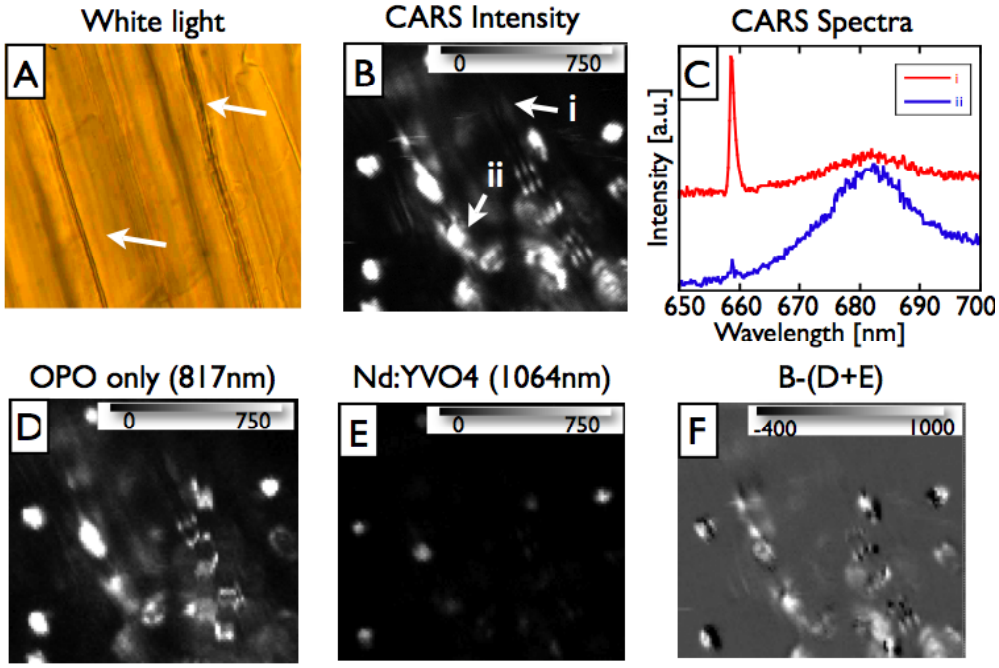

Fig. 2. (A) Transmitted light micrograph of the lower stem near the roots (hypocotyls region) of a living *Arabidopsis thaliana* seedling. (B) Intensity CARS image of the same area of the hypocotyls shown in (A). The areas highlighted by arrows in the image are areas where emission spectra were taken and correspond to the spectra shown in (C). Image scale is 40 µm x 40 µm. (C) Local emission spectra obtained by positioning the laser beams to different parts of the plant cell as indicated in (B). (D) Two-photon-excited confocal autofluorescence image of the same plant area, where just the picosecond OPO beam (817 nm) was used to excite fluorescence. (E) Same as (D), but with just the Nd:YVO_4. (F) Difference image, where the fluorescence images shown on (D) and (E) were subtracted from the "CARS" image in (B). This should result in a CARS image essentially free of background fluorescence contributions except for those due to simultaneous absorption of 1 photon from the pump beam and 1 photon from the Stokes beam. All CARS images were taken at 256 x 256 pixels with 2 ms dwell time per pixel, resulting in a total image acquisition time of 6.93 min.

To determine the extent of the fluorescence contributions to the image shown in Fig. 2(b), the same area of the sample was also scanned by alternately blocking each one of the two

lasers that are needed to generate a CARS signal. The image in Fig. 2(d) shows an autofluorescence micrograph obtained by scanning the sample with OPO laser excitation only, while the image shown in Fig. 2(e) results from Nd:YVO_4 laser excitation only. In order to try to eliminate the autofluorescence background contributions from the CARS image, the independently acquired fluorescence-only images (Fig. 2(d,e)) were then subtracted from the combined CARS image (Fig. 2(b)), resulting in a "corrected" CARS image (Fig. 2(f)) free of two-photon excited fluorescence from the individual beams, but not accounting for fluorescence contributions excited due to frequency mixing of the pump and Stokes beams.

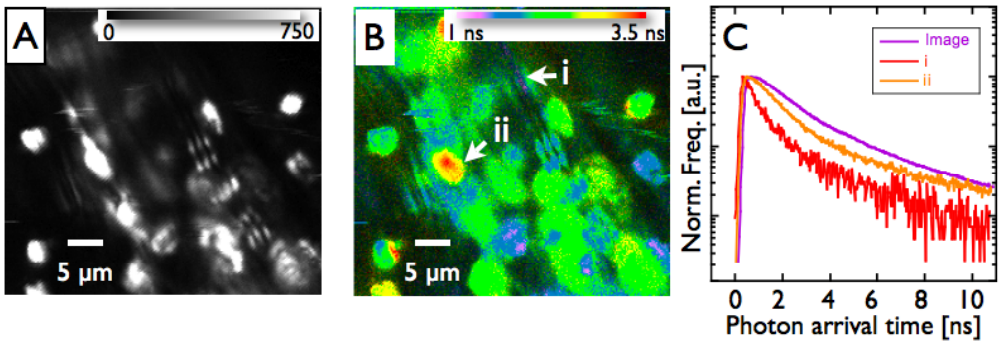

Fig. 3. Time-correlated CARS micrographs of the hypocotyl of an *Arabidopsis thaliana* seedling. (A) Intensity CARS image showing all photons collected per pixel without arrival time information. Image scale is 40µm x 40µm. (B) This image shows the same area as in A, but encodes the photon arrival time in false color. Note that some well-confined areas of the image indicate very short photon arrivals times (shown in dark-blue to purple color). (C) Normalized arrival time decays for different regions highlighted by the arrows in (B), as well as averaged over the entire image. The CARS images were taken at 256 x 256 pixels with 2 ms dwell time per pixel, resulting in a total image acquisition time of 6.93 min.

Alternatively, using TCSPC electronics, the photon arrival time can be used to determine fluorescence and CARS contributions to the image contrast. Fig. 3(a) shows the same intensity-only CARS image of the plant seedling as shown in Fig. 2(b). In comparison, the image in Fig. 3(b) shows photon arrival time information encoded by false color. Parts of the image exhibiting purple-blue colors represent signal dominating from photons that arrive within ~ 1 ns of the laser pulse, while green-red color represents the arrival of "delayed" photons. The photon arrival time plots in Fig. 3(c) show photon arrival time decays ("lifetime plots") obtained from the same areas (i) and (ii) highlighted in Figs. 2(b) and 3(b), as well as the average over the entire image.

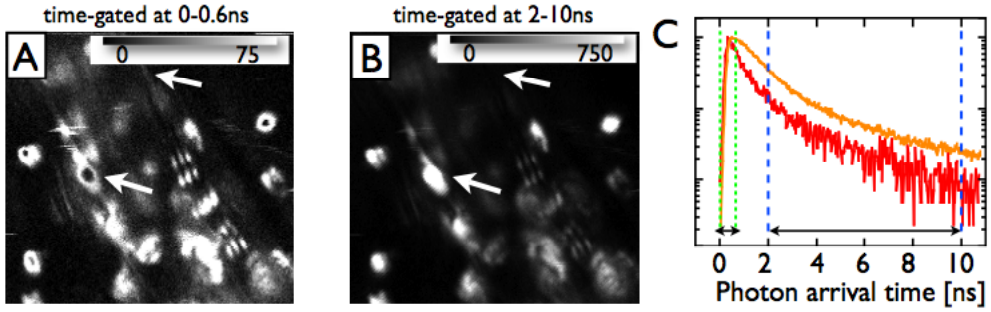

Fig. 4. Time-gated CARS microscopy images of the same hypocotyls as shown in Figs. 2 and 3. (A) Intensity image with a time gate set to 0-0.6 ns. This short time gate separates the instantaneously arriving CARS photons from the delayed photons due to fluorescence emission. The gate width is set to cover all photons that are emitted within the time set by the instrument response function. (B) Intensity image with time gate set between 2-10 ns. This image shows only two-photon excited fluorescence. (C) Normalized arrival time decays for different regions overlaid with the schematic times gates used for isolating "early" and "late" photons resulting in the images shown in (A) and (B). The CARS images were taken at 256 x

256 pixels with 2 ms dwell time per pixel, resulting in a total image acquisition time of 6.93 min.

In Fig. 4 we make use of the additional information provided by also registering photon arrival times. Here, software time-gates were used to generate the image contrast. The image in Fig. 4(a) shows the same image of the plant hypocotyls shown in the previous figures, but only photons arriving within 0-0.6 ns of the laser pulse were used to generate the image contrast. The time gate is indicated by the green dashed lines in the photon arrival time plot in Fig. 4(c). Figure 4(b), on the other hand, shows the same image generated by counting only those photons arriving between 2-10 ns after the laser pulse (represented by the blue dashed lines in the photon arrival time plot). White arrows show the same sample locations as in the previous figures.

3.2. Rat artery sample

CARS images of a rat artery sample were acquired by scanning a small part of the arterial wall and the lumen with an image size of 30 x 30 µm at 256 x 256 pixels resolution, and 0.6 ms dwell time per pixel. The OPO wavelength was tuned to the aliphatic C-H stretch mode at 2845 cm^{-1} corresponding to a pump wavelength of 816.8 nm. Here, the pump beam was 15 mW at the sample and the Stokes beam 10 mW at the sample.

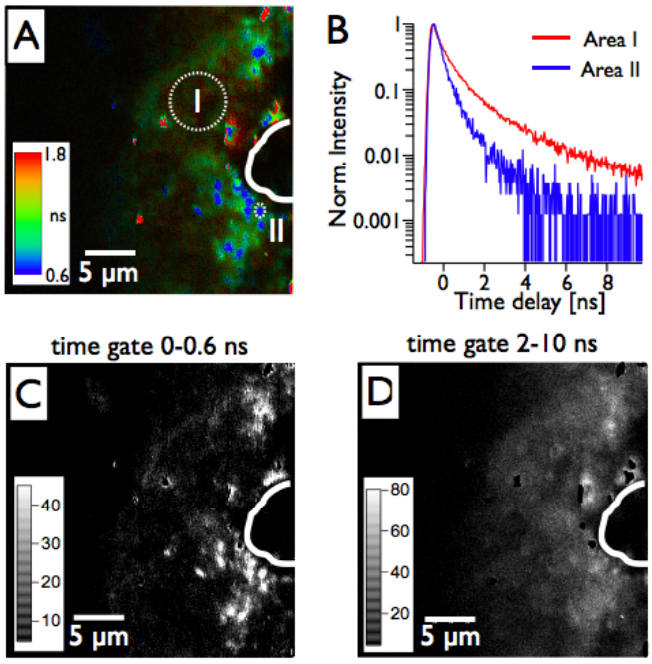

Fig. 5. CARS micrograph of rat arterial tissue (cross-section) showing the effect of time-gating on animal tissue. The fat white outline drawn in the image indicates the border between the tissue and the beginning of the interior of the artery (the"lumen"). (A) CARS image encoding the photon arrival time on a false color scale. Image scale is 30 x 30 µm. (B) Normalized photon arrival time histograms obtained by isolating areas with short photon arrival times from areas with long photon arrival times as highlighted by white circles in (A). (C) Intensity image with a time gate set to 0-0.6 ns, covering the instantaneously emitted CARS photons. (D) Intensity image with time gate set to 2-10 ns, which captures all delayed photons due to fluorescence emission. Some areas of the sample shown by brightly red-colored spots lead to saturation of the detection electronics, and photon arrival times could not be properly represented for these areas. These parts were set to black in (C) and (D). All CARS images are acquired at 256 x 256 pixel resolution with 0.6 ms dwell time per pixel and a total image acquisition time of 2.03 min.

The image shown in Fig. 5(a) shows a false color-encoded representation of the intensity and arrival time of the signal detected at 658 nm wavelength. Similar to the plant sample image, areas with different photon arrival times can be identified, in particular small areas surrounding the lumen of the artery with average photon arrival times of ~0.6 ns. Representative photon arrival time decay plots for the areas labeled (I) and (II) and highlighted by white dashed outlines in Fig. 5(a) are shown in Fig. 5(b). Local emission spectra (not shown) additionally identify the areas representing fast photon arrival time decays as stemming from CARS signals as characterized by narrow-band emission peaks, whereas areas with delayed photon emission exhibit broad spectral fluorescence emission. Software time-gating can again be employed to separate photons arriving within the intrinsic instrument response of the system from delayed fluorescence photons. Figure 5(c) shows an intensity image of all the photons arriving within 0 - 0.6 ns of the laser pulse. The image in Fig. 5(d), on the other hand, shows an image representing all photons arriving within 2-10 ns after the laser pulse.

4. Discussion

CARS signals are essentially instantaneous - at least on time scales measurable with electronic photon counting equipment - while fluorescence signals decay with time constants on the nanosecond scale. Time-gating with fast optical gates would allow us to optimally separate both signal sources, but such devices typically lead to substantial signal loss and are currently not very practical for use in microscopy. Because of the time-scales involved, software time-gating using TCSPC data is much more practical and efficient for this application. In this case, however, even though one would prefer to extract the CARS signal by setting a time gate of less than 1 ps, in practice it is limited by the timing uncertainty of the detectors and electronics used in the system. The overall time resolution of a detection system is a convolution of a number of factors, e.g. the time resolution of the detector, individual TCSPC components, and the excitation source. In our setup, the main limiting factor to the system response time is the SPAD time resolution with an IRF specified to be approximately 300 ps, since all other sources have a timing uncertainty of < 35 ps. In order to determine the intrinsic timing jitter of our system for the CARS signal, we measured the system response time by generating a CARS signal in the absence of fluorescence contributions. With pump and probe laser wavelengths set to 816.8 nm and 1064 nm, respectively, the CARS signal is centered at 658 nm. Traditionally, the system IRF is measured by reflecting a tiny fraction of laser light back through the microscope onto the SPAD detector and acquiring a photon arrival time histogram. For our CARS system, this approach is not applicable because the pump and probe laser beams have wavelengths that are significantly red-shifted when compared to the CARS signal wavelength. SPAD detectors, however, are known to have - amongst other sources leading to an increase in timing uncertainty - a wavelength-dependent response. And, indeed, when we determined the IRF by reflecting the primary laser beams onto the SPAD, we found the IRF at 816.8 nm to be ~ 1 ns, while it is > 2 ns at 1064 nm. Only the CARS signal measured at 658 nm results in an IRF of 310 ps, which matches the timing jitter specified in the manufacturer's data sheet. Based on this intrinsic decay time, we chose to set our time gates for all images to ~ 2x the IRF, i.e. from 0-0.6 ns, in order to capture most CARS photons, while still providing significant rejection of fluorescence photons. Another, interesting feature of SPADs is that they count single photons, i.e. once a photon has been detected, the detector is dead and cannot detect any other photons for ~ 35 ns. Thus, even in the presence of very high fluorescence levels, these detectors can effectively isolate the CARS signal because of its instantaneous nature. This means that TCSPC-based techniques are well suited for conducting experiments in regimes with low signal versus background count rates as long as the difference in signal arrival times is significant.

To demonstrate the benefits of CARS signal time-gating, we imaged tissues that are known to exhibit significant autofluorescence within the CARS signal emission band near 658 nm. Figures 2-4 show this on the example of plant tissue where the main source for autofluorescence can be attributed to chlorophyll emission. The contribution and magnitude

of fluorescence to the CARS signal is only apparent when comparing local emission spectra as shown in Fig. 2(c). These reveal that the apparent "CARS" signal in Fig. 2(b) is largely convoluted by fluorescence contributions. It should be noted that even though the spectrum obtained in area (ii) shows an intensity ratio of <10:1 of autofluorescence over CARS, the actual photon count ratio detected ranges from 100:1 to 1000:1 as a result of the wide autofluorescence band from chlorophyll in the plant organelles. Typically, one would try to employ narrow spectral bandpass filters that isolate the CARS signal and minimize background contributions from the broad fluorescence, but even then, the background contributions can be equal to or overwhelm CARS signals. Another potential approach to reducing the fluorescence background is demonstrated in Fig. 2(f), where fluorescence images obtained by scanning the sample with only one of the two laser beams (Fig. 2(d) and Fig. 2(e)), respectively, were obtained separately and then subtracted from the "CARS" image (Fig. 2(b)) obtained with both lasers simultaneously present. This approach, however, is typically not very practical since it requires taking several different time-consuming image scans of the same sample location while the sample must remain stationary at all times throughout the imaging process. The result of this subtraction process is shown in Fig. 2(f), where due to sample drift during the acquisition of the successive image series, some areas exhibit inverted contrast. This technique also does not account for fluorescence excitation due to frequency mixing of the pump and probe beams.

The additional information gained by recording photon arrival time information is demonstrated in Fig. 3. Here, the "CARS" intensity image (Fig. 3(a) - same as Fig. 2(b)) is overlaid with the average photon arrival time for every pixel encoded by false color as shown in Fig. 3(b). The photon arrival time histograms shown in Fig. 3(c) illustrate this even more by representing the local decay curves collected in areas (i) and (ii) as indicated in Fig. 3(b) and comparing them to the average over the entire image. By comparing this information with the local spectroscopy in Fig. 2(c), it is quite apparent, that areas with high CARS signal emission (indicated by the intense, narrow peak at 658 nm) correlate with areas of short photon arrival time (indicated by the blue color in Fig. 3(b), and the fast decay curve in Fig. 3(c)).

Thus, by employing software time-gating, where photons with a microscopic arrival time of <0.6 ns are separated from photons with an arrival time >2 ns, we can generate a "pure" CARS image as shown in Fig. 4(a). The corresponding image due to fluorescence emission is shown in Fig. 4(b). The time gates are schematically shown by the green dashed lines (CARS time gate) and the blue dashed lines (fluorescence time gate) shown in Fig. 4(c). A potentially even better, but more computation-intensive approach could be taken by fitting the decay curve for every pixel with a double-exponential decay curve consisting of a short decay time (representing CARS signals) and a slightly longer decay time (representing fluorescence signals). The CARS and fluorescence images could then be constructed by plotting the amplitudes of each exponential decay in separate images, respectively. We also tested this approach to see if it might further improve the image separation, but the image contrast was quite similar to that obtained by simply sorting early and delayed photons and plotting the respective count rates. As can be seen by the contrast in Fig. 4, CARS signals due to aliphatic lipid vibrations primarily originate in the membrane of plant cells. This is particularly apparent in Fig. 4(a), where some organelles such as the one shown near the center of the image (highlighted by an arrow) now exhibit a CARS-signal free interior, as expected for a plant organelle that is rich in lipids. Since membranes composed of a single lipid bilayer provide rather weak CARS contrast we tentatively assign these structures to lipid-rich plastids, possibly being a precursor to the folded thylakoid membranes found in chloroplasts, which haven't fully developed yet because these plants were dark-grown. This particular contrast could also be caused by the nature of our detection system, i.e. epi-CARS, which is only sensitive to objects smaller then the wavelength as well as interfaces [11], but as shown by Evans et al., CARS signal generation in tissue leads to substantial back-reflection of the forward-scattered CARS signal and thus a convolution between forward and epi-CARS signals [1]. The entire organelle, however, leads to significant fluorescence emission (see Fig.

4(b)), indicating that it is rich in chlorophyll. It should be noted that these images represent an arbitrary section through the hypocotyls of the *Arabidopsis thaliana* seedling, which is difficult to control because it was obtained by scanning the intact, living plant.

Another example of the efficacy of applying photon arrival time-gating to the imaging of a targeted chemical species in the presence of autofluorescence contributions is shown in Fig. 5. Here, the sample is a cross-section of a healthy rat artery. Again, when tuned to the aliphatic lipid CH stretching mode, a response from all tissue lipids is expected, but this will be convoluted with autofluorescence contributions, in this case primarily due to porphyrin and heme fluorescence emission. Surprisingly, the photon arrival time image shown in Fig. 5(a) indicates the presence of a number of small, discrete regions within the tissue near the lumen that exhibit very strong lipid vibrations. These regions exhibit photon arrival time decays comparable to the IRF of our system (~310 ps), as indicated by the histogram plots shown in Fig. 5(b), and again, strong CARS signals in these areas are confirmed by an intense, spectrally narrow peak occuring at 658 nm (not shown). We tentatively assign these areas to temporary small, lipid-rich deposits as rats do not typically suffer from cardiovascular disease and their associated saturated fatty acid deposits. The spatially limited extent of these areas is again highlighted when we employ time-gating to separate CARS signals from autofluorescence contributions (Fig. 5(c) and Fig. 5(d) respectively).

5. Conclusions

We have shown how CARS microscopy can benefit from simultaneously collecting photon arrival time information using time-correlated single photon couting. This particular concept represents a straight-forward upgrade to most CARS microscopes that use photon-counting detectors based on commercially available upgrade kits for confocal microscopes. The use of software time gating can then be used for the temporal separation of CARS signals from background autofluorescence in tissue. Issues resulting from background autofluorescence have not yet been widely addressed in the current CARS microscopy literature, but, depending on the type of tissue, can lead to substantial background contributions on top of other sources of background (e.g. the widely acknowledged non-resonant CARS signal). We have confirmed the CARS nature of areas isolated in time-gated CARS microscopy by also collecting local emission spectra, which exhibit strong, narrow peaks at the wavelength expected for the CARS signal. The signal strength of these CARS signals, however, is comparable to the integrated fluorescence signals when collected through relatively wide bandpass filters, which is current practice, because it allows the collection of several different CARS signals over a narrow tuning range without having to change filters. Employing more narrow bandpass filters, however, will only partially improve the CARS contrast, because it is still convoluted with contributions from the broad fluorescence background. Spectral deconvolution of narrow CARS signals from broad autofluorescence is an option, but typically requires the simultaneous acquisition of images at several different wavelengths or the acquisition of spectra for every pixel resulting in very large data files. Such deconvolution also becomes increasingly less efficient if the CARS signal is relatively weak compared to the fluorescence background. Separating such weak CARS signals from autofluorescence is the true strength of time gating. We expect this to become more and more important as CARS microscopy moves towards in-vivo applications. Currently, image acquisition times are limited by the pixel dwell times needed for single photon counting. This can still be realized and combined with most fast (galvo-scanner based) CARS imaging schemes reported in the literature through the addition of commercial FLIM upgrades, but will require several image sweeps to optimize the signal-to-noise ratio. Ideally, however, novel, fast optical gating schemes could be employed that better separate the different signal contributions which will be compatible with both scanning as well as widefield imaging approaches to CARS microscopy. This leaves significant room for future development.

Acknowledgements

We would like to thank Yi-Shin Su and Prof. J. Clark Lagarias from the UC Davis Section of Molecular and Cellular Biology, College of Biological Science, for providing the *Arabidopsis thaliana* sample, and Rajesh Raman and Chris Pivetti, UC Davis Health System, for providing the rat artery cross section. We would further like to thank Prof. Daniel Côté, Canada Research Chair in Biophotonics, Université Laval, for his help and valuable suggestions. This work was supported by funding from the National Science Foundation. The Center for Biophotonics, an NSF Science and Technology Center, is managed by the University of California, Davis, under Cooperative Agreement No. PHY 0120999. T. Huser also acknowledges support by the Clinical Translational Science Center under Grant Number UL1 RR024146 from the National Center for Research Resources (NCRR) a component of the National Institutes of Health (NIH), and the NIH Roadmap for Medical Research. J.W. Chan acknowledges support from the LLNL Laboratory-directed Research and Development Program. Work at LLNL was performed under the auspices of the U.S. Department of Energy by Lawrence Livermore National Laboratory under Contract DE-AC52-07NA27344.